Q-factor inversion using reconstructed source spectral consistency

Matan Shustak[1] and Ariel Lellouch[1]

ABSTRACT

Seismic waves propagating in an anelastic medium undergo phase and amplitude distortions. Although these effects may be compensated for during imaging processes, a background Q-model is generally required for their successful application. We have developed a new approach to the Q-estimation problem, which is fundamentally related to the basic physical principle of time reversal. It is based on back-propagating recorded traces to their known source location using the reverse tomographic equation. This equation is a ray approximation of viscoelastic wave propagation. It is applied assuming a known and correct velocity model. We subsequently measure consistency between spectral shapes of traces that were back-propagated using the tomographic equation. We formulate an inverse problem using this consistency as an objective function. In conventional inversion, on the contrary, the discrepancy between modeled and recorded data, or some data characteristics, is minimized. The inverse problem is solved by ant-colony optimization, a global optimization approach, to avoid local minima present in the objective function. This method does not require knowledge of the source function and uses the full spectrum rather than its parametric reduction. Through synthetic and field cross-hole examples, we illustrate its accuracy and sensitivity in inverting for complex attenuation models. In the synthetic case, we also compare reconstructed source consistency with the conventional centroid frequency shift objective function. The latter displays poor resolution when recovering complex Q structures. We determine that the reconstructed source-consistency approach should be used as a part of an iterative workflow, possibly yielding initial models for a joint velocity and Q inversion.

INTRODUCTION

The subsurface medium is anelastic in nature, and seismic waves propagating through it lose some of their energy to heat, inducing amplitude and phase distortion (Aki and Richards, 2002). Such attenuation effects can be quantified using the quality factor Q, and they account for traveled distance, propagation velocity, and the signal's frequency content. In the subsurface, Q values are connected to lithology, porosity, and pore-fluid characteristics (Wang et al., 2015). Throughout the manuscript, we make the common assumption of frequency-independent Q within the seismic band, following Liu et al. (1976) and Kjartansson (1979).

High-resolution seismic data are important for detailed reservoir description, time-lapse applications, and spatial variation recovery of porosity, gas content, and pore pressure. However, recorded data suffer from attenuation and have lower frequency content. To compensate for attenuation, in terms of phase and amplitude, inverse Q filtering may be applied given a reliable estimate of the subsurface Q model (Wang, 2006). Such a procedure is gaining increasing popularity because it offers the promise of increasing the local frequency content of the recorded data (van der Baan, 2012).

In conventional seismic surveys, Q is rarely measured directly (Blias, 2012). If a well has been drilled, different seismic methods may be used for Q estimation (Tonn, 1991; Harris et al., 1997). Nonetheless, they are inherently confined to a local measurement and do not encapsulate horizontal variation. Derivation of Q from seismic data using inversion methods is widely studied and used. These techniques usually belong to one of two groups — wave-equation or ray-approximation-based. Wave-equation methods (Shen et al., 2015; Dutta and Schuster, 2016) solve the physically accurate nonlinear relations, whereas ray-based techniques (Brzostowski and Mcmechan, 1992; Quan and Harris, 1997; Hu et al., 2011) assume a linear relation between measured data and Q^{-1}.

Regardless of their implementation, conventional inversion methods are based on misfit minimization. It is usually measured in terms of the difference between recorded and modeled data (or data

characteristics). In recent studies aiming at Q-model inversion, frequency-based criteria, such as the centroid frequency shift or log spectral ratio (Wang et al., 2016), are the common choice. For full-waveform inversion (FWI)-type methods, trying to simultaneously invert for propagation velocity and Q (Malinowski et al., 2011), the objective function is minimal discrepancy between modeled and recorded data. Despite their differences, Q-inversion and FWI-type methods require knowledge of the source function, which is difficult to measure or estimate.

In this study, extending earlier work (Shustak et al., 2017), we suggest a new method that would directly eliminate the need for source function knowledge. The method is based on back-propagating recorded data to their known original location using a viscoacoustic inverse tomographic equation. For this, we assume the used velocity model is correct. Such an assumption is often made in the Q-inversion literature, especially in the ray-based case (see, e.g., Quan and Harris, 1997; Wang, 2009; Cavalca et al., 2011; Hu et al., 2011). The velocity model is either accepted from an outside method or estimated as a separate step, independent of Q, during the inversion. The strong coupling between velocity and Q has been recognized and studied by different authors. For example, Carcione et al. (2002) describe both as a function of the same complex elastic modulus, leading to inherent coupling. During wave propagation, Q affects traveltimes through dispersion. On the other hand, amplitude losses due to viscoelastic effects are influenced by wavepaths, which themselves depend on the velocity model (Mulder and Hak, 2009; Hak and Mulder, 2011). As a consequence, it is practically difficult to simultaneously invert for both fields (Ribodetti et al., 2000; Kurzmann et al., 2013). Some authors (da Silva et al., 2017) suggest that a crude Q model may be practically sufficient for inversion and thus may mitigate the problem. However, for this study, we will assume that the velocity model is correct and estimate Q only. In the "Discussion" section, we suggest a more complete workflow aimed at handling coupling issues.

For back propagation, data are sorted into common-shot gathers. They are then back-propagated along raypaths calculated using an acoustic velocity model. Their propagation is compensated for anelastic losses by using an estimated, or trial, Q model, along the calculated raypaths. If this Q model is correct, the reconstructed spectral shapes of all traces originating from the same source will be similar to one another. Accordingly, we use spectral consistency of all traces back-propagated to the same origin location as an objective function. This approach is closely related to the time-reversal focusing principle (Lellouch and Landa, 2017, 2018; Shustak and Landa, 2017). It uses the entire source spectrum, eliminates the need of source function knowledge, and avoids the common Q-inversion approach of minimizing the discrepancy between characteristics of recorded and modeled data, which we later show to suffer from low resolution.

Because the objective function is nonconvex, local optimization methods are bound to reach a local minima. Therefore, we use ant colony optimization (ACO), a probabilistic global optimization technique (Dorigo and Gambardella, 1997) for solving the Q-estimation inverse problem. We present a ray-based, relatively straightforward, and simple back-propagation approach. Nonetheless, the same concepts may be formulated in a wave-equation framework.

In the following, we begin by formulating the inverse tomographic equation and list assumptions made in its development. We then use the tomographic equation for source reconstruction and

formulate its spectral consistency as an objective function. We analyze the objective function's sensitivity to Q and velocity using a simple two-layer toy model. Then, a global optimization solution to the inverse problem, the ACO, is briefly discussed. Details of the method and tuning parameters are described in Appendix A. Using a 2D cross-hole synthetic example, we demonstrate the inversion workflow and compare it with a conventional frequency-shift approach. Results of our suggested method are much closer to the true model. We also illustrate its quality by displaying reconstructed spectra and data misfit between recorded and modeled data. For completeness, we analyze the stability of the suggested inversion approach as a whole, and we show its superior robustness compared with a conventional frequency-shift-based method. Finally, we apply the reconstructed source consistency method to a challenging 2D cross-hole field data from southern Israel.

RECONSTRUCTED SOURCE CONSISTENCY

Source-frequency reconstruction is the basis of the suggested inversion scheme. In the most general case (Liner, 2012), the relation between the recorded spectrum $R(f)$, source spectrum $S(f)$, frequency-independent effects G, absorption (or intrinsic attenuation) effects $H(f)$, receiver response $M(f)$, and extrinsic attenuation $I(f)$, is

$$R(f) = G \cdot S(f) \cdot H(f) \cdot M(f) \cdot I(f). \tag{1}$$

Extrinsic attenuation $I(f)$, in contrary to intrinsic attenuation, preserves energy. However, in the presence of subsurface layering and/or scatterers, recorded wavefields will effectively undergo frequency-dependent extrinsic attenuation (Liner, 2012). In this, case, energy scattered due to structural elements is disassociated from recorded wavefronts, despite not being lost to heat.

In this study, we assume, following Quan and Harris (1997), the following linear relation:

$$R(f) = G \cdot S(f) \cdot H(f). \tag{2}$$

The first used assumption is a flat receiver response within the frequency range of interest, so that $M(f) \rightarrow M$ and can be incorporated into G. A second assumption is that extrinsic attenuation effects are unaccounted for, and all elastic-propagation effects (geometric spreading, mode conversion, transmission/reflection coefficients, scattering, etc.,) may be described by the frequency-independent function G. Assuming a low-loss solid ($Q > 5$), we can write (Aki and Richards, 2002)

$$H(f) = e^{-\alpha_0 f}, \qquad \alpha_0 = \frac{\pi l}{QV}, \tag{3}$$

with V being the propagation velocity and l being the propagation distance. Hence, we use the tomographic equation to estimate the recorded spectrum along a known raypath:

$$R(f) = G \cdot S(f) \cdot e^{-f \int_{\text{ray}} \frac{\pi}{QV} dl}, \tag{4}$$

where dl is an incremental traveled distance along the ray and V is the propagation velocity at dl. It is important to note that this formulation is ray based, i.e., assuming a single propagation mode of infinite frequency. For this study, we elect to use first-arrivals (P-waves) only.

Therefore, when applied to seismic data, muting around the first arrivals must be conducted.

We show the application of the forward tomographic equation on a single source (Figure 1). The velocity and Q are realistic for a shallow subsurface environment. The recorded spectrum significantly differs from the original one, and the effects of highly absorptive layers are clearly visible.

Because we assume frequency-dependent attenuation depends solely on anelastic absorption, normalizing the reconstructed source spectrum eliminates all elastic effects (G). Therefore, the normalized back-propagated source spectrum is

$$S(f) = R(f) \cdot e^{f \int_{\text{ray}} \frac{\pi}{QV} dl}. \quad (5)$$

This is the reverse tomographic equation. In other words, $S(f)$ can be regarded as the spectral shape of the reconstructed source. It is a function of recorded frequency spectrum $R(f)$, attenuation model Q, and medium velocity V. Velocity also influences source-receiver raypaths, calculated using acoustic ray-tracing and along which the tomographic equation 5 is applied. If we assume that the velocity model is correctly estimated using conventional methods, the only remaining unknown is the attenuation model Q. As expected, different Q models yield dissimilar reconstructed source spectra, as we illustrate in Figure 2.

We suggest using the reconstructed source spectrum $S(f)$ as an objective function for Q model inversion. Let us begin by observing a single shot record with multiple receivers. Given a correct attenuation model, the reconstructed source spectrum has to be the equal for all back-propagated recorded traces. This is due to the intangible time-reversal physical property (Lellouch and Landa, 2018) and does not induce any assumption regarding the source. However, it does require the instrumental response of all receivers to be equal or accounted for, which is inherently assumed in any estimation method. Quantitatively, similarity between different spectra may

be defined using one of the many known coherency measures. In this study, we chose to minimize the variance between all back-propagated traces of the same shot. Because shots may differ from one another, we only average coherency values over different sources and do not require them to have the same spectrum. The objective function is formulated by

$$E(Q) = \sum_{s=1}^{N_{\text{shots}}} \sum_{f=f_{\text{min}}}^{f_{\text{max}}}$$

$$\times \sqrt{\frac{1}{(N_r^s - 1)} \sum_{i=1}^{N_r^s} \left[S_i^s(f, Q) - \frac{1}{(N_r^s)} \sum_{j=1}^{N_r^s} S_j^s(f, Q) \right]^2},$$

$$(6)$$

where $S_i^S(f, Q)$ is the reconstructed source spectrum for the ith receiver of the sth source, Q is the attenuation model, N_r^s is the number of receivers for the sth source, and N_{shot} stands for the total number of shots. The variance is calculated within a selected frequency band $\{f_{\text{min}}, f_{\text{max}}\}$, in which there is significant information content. Choosing a limited frequency band also avoids instability that may arise from the exponential term in equation 5.

Figure 3 illustrates the sensitivity of the chosen objective function E in a simple cross-hole acquisition of a two-layer model (Figure 3a). For this analysis, we vary Q and velocity V. In the forward-modeling stage, data are generated using the tomographic equation with the true Q and velocity models. Therefore, the ACO objective function, which is $1 - E(Q, V)^{1/4}$, should be one for the correct model parameters. In Figure 3b, we show the objective function's sensitivity to different Q value errors. Although the maximal value is indeed obtained at the true Q value, the objective function's shape is worth analyzing. First, there are several visible local maxima (pointed by the arrows), indicating possible difficulties using local optimization
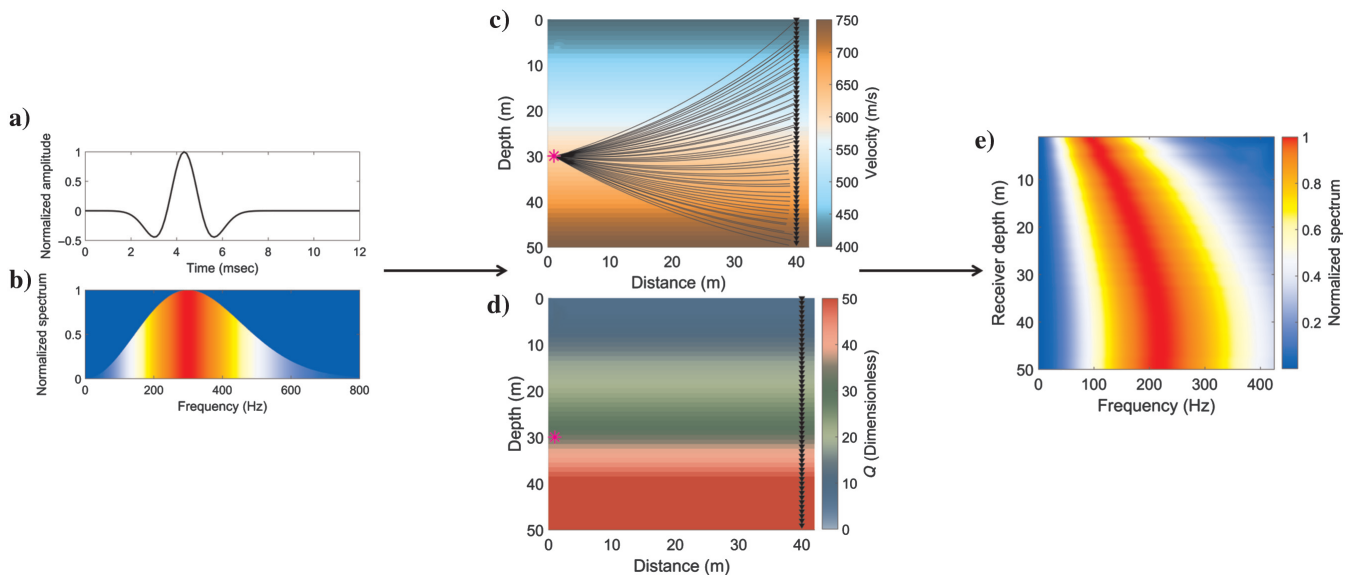

Figure 1. Illustration of the forward tomographic equation for a single source. A source wavelet is shown in (a) and its frequency spectrum in (b). The velocity model, a 1D model increasing with depth, is shown in (c). Raypaths from the source (magenta star) to receivers (black triangles), along which the tomographic equation is calculated, are superimposed on the velocity model. The Q-factor model is shown in (d). The spectrum of the recorded signal at the receivers shows the dissipative effects of the lower Q layers (e).

methods. In addition, the function changes very slowly in certain directions, which is indicative of a high condition number. Thus, convergence rates of local optimization methods are expected to be low. Although we assume that the velocity is correct throughout this study, we also analyze the objective function's sensitivity to velocity errors (Figure 3c). From this plot, it can be seen that the objective function is more sensitive to velocity than Q. Errors of more than 5% of the velocity turn the method practically useless, whereas such errors for Q still yield very high objective function values. This observation is illustrative of the strong $Q - V$ coupling discussed in the "Introduction" section.

For both cases, the objective function does not decrease symmetrically with error percentage. Instead, it follows a preferred orientation, more accentuated in the Q sensitivity plot. For this example, errors with the same sign (either positive or negative) are less penalized by the objective function than errors of inverse sign (one positive and one negative). Because of the cross-hole acquisition setup, errors do not cancel out. In surface-based surveys, on the contrary, errors often compensate for one another if they are of opposing directions. Based on this simple example, we draw several general observations — Q inversion using this objective function is challenging and has a higher chance of success using global optimiza-
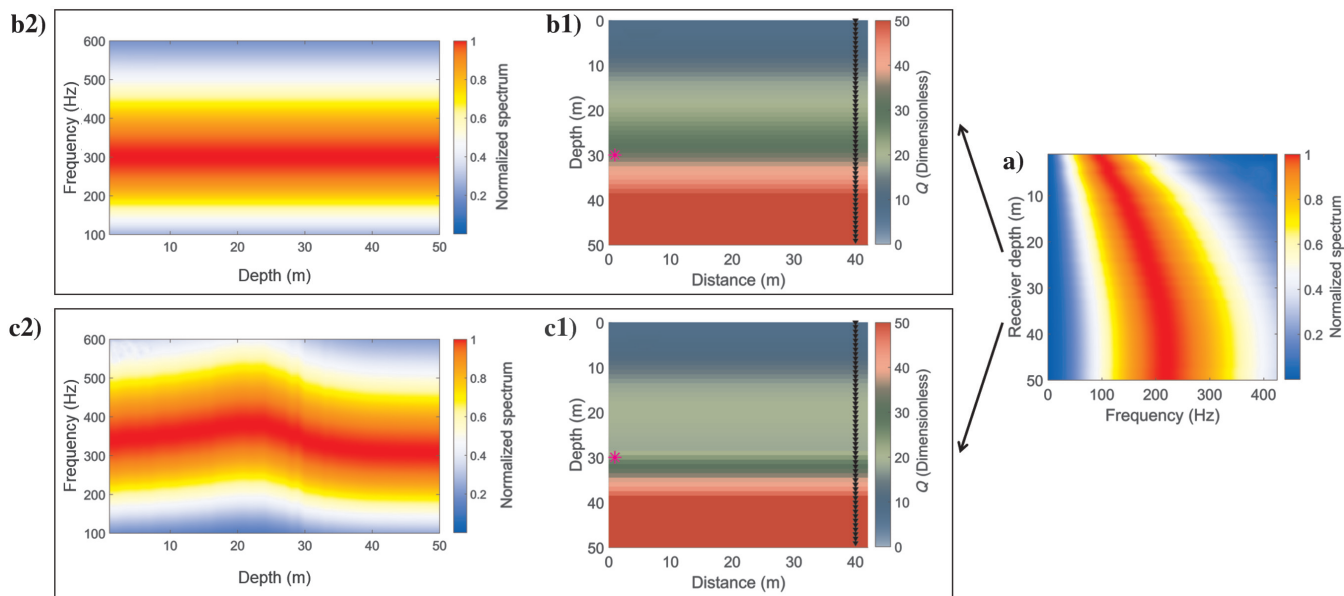

Figure 2. Illustration of the normalized backward tomographic equation. The recorded shot's spectrum, recorded by receivers at different depths, is shown in (a). Due to different raypaths and Q along them, its shape depends strongly on depth. The recorded spectrum is used for the backward tomography equation using the (b1) true and (c1) a weakly erroneous Q-factor model. The shape of the spectrum, reconstructed at the source location, is consistent among all receivers (b2) for the correct Q-factor model (b1). When a wrong model is used (c1), the effect on the reconstructed spectrum is visible and it becomes incoherent along receivers (c2).
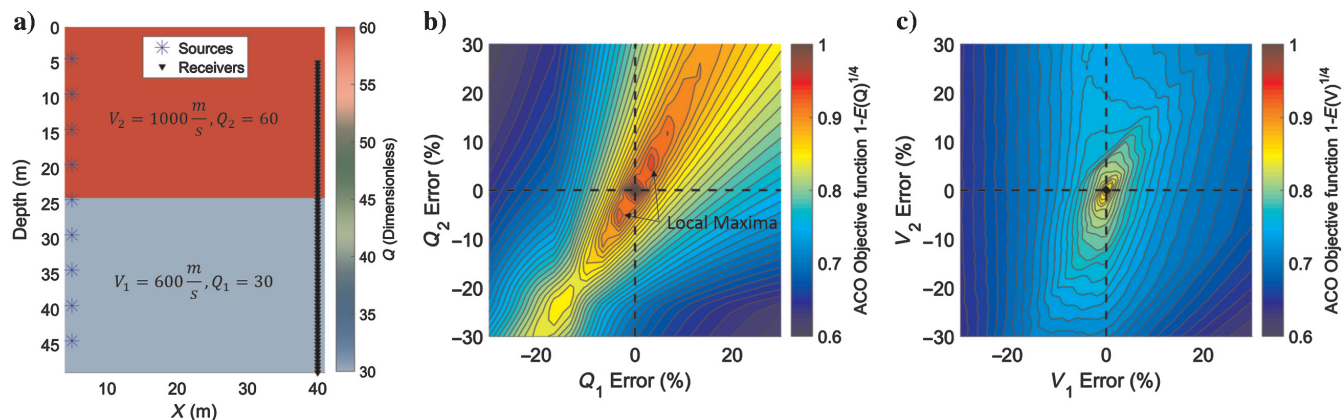

Figure 3. Objective function sensitivity to Q and velocity. A simple two-layers viscoacoustic model, with cross-hole acquisition, is shown in (a). Sources are denoted by blue asterisks and receivers by black triangles. Assuming the correct velocity model, (b) shows the sensitivity of the ACO objective function to Q errors. Although the maximal value is obtained at the true Q values (denoted by the cross), there are several local maxima, denoted by arrows. In (c), we show the objective function's sensitivity to velocity, assuming the correct Q model. The objective function is much steeper, and it does not have local maxima. For (b) and (c), there is a preferred orientation to the objective function — errors of different signs are more penalized than errors in the same direction.

tion. Nonetheless, it is bound to fail without an accurate enough velocity model.

GLOBAL OPTIMIZATION USING ACO

The functional $E(Q)$ may be used as the objective function in an inverse problem formulation. It is calculated using the entire spectrum of the seismic band. In conventional centroid frequency-shift or log-spectral ratio tomography, a simple parametric reduction of this spectrum is used instead. Due to the complexity and nonuniqueness of the objective function $E(Q)$, we advocate the use of global optimization methods. Although they are more computationally demanding and require adequate model parameterization, they can avoid local extrema and find the overall best solution to the inversion problem. There is a very large variety of global optimization algorithms, each with its own advantages and limitations. Initially, inversion was conducted using the very simple and fast simulated annealing (Landa et al., 1989), but it did not converge within reasonable run times due to objective function complexity. We therefore opted for a more advanced method, ACO. However, there are many other possible metaheuristic approaches, such as genetic algorithms, particle swarm optimization, or neighborhood algorithms (Sen and Stoffa, 2013), which we expect to perform similarly well.

ACO, derived by mimicking the behavior of foraging ants, was introduced by Dorigo (1992) and Dorigo and Gambardella (1997) in its discrete form, and it was later extended to the continuous domain (Socha and Dorigo, 2008). Ants start by randomly searching the area around their nest for food. Once an ant finds a source of food, it evaluates it and carries some of it back to the nest, while leaving a pheromone trail indicative of the amount and type of the remaining available food. The pheromones serve as a tool for indirect communication between ants and enable them to find the optimal path to the food source. This behavior has been interpreted as a probabilistic approach in which pheromone intensity guides the exploration of the search space. In other words, the probability of exploring a certain point in the search space depends on previous objective function satisfaction at that point. Uncharted points in the search space are randomly explored following a uniform distribution. A more detailed explanation of the method, as well as tuning parameters, is found in Appendix A.

SYNTHETIC DATA EXAMPLE

We demonstrate the application of the method on a synthetic cross-hole example. The acquisition setup, along the underlying velocity model and representative source-receiver paths, are shown in Figure 4. It is important to note that the model is structurally complex, thus inducing extrinsic attenuation effects. We chose to illustrate the method on a case in which direct source-receiver paths are present, in contrary to conventional reflection acquisition. The suggested approach can be applied to any type of survey. Thanks to the inverse tomographic equation formulation, the only requirement is a computed set of raypaths connecting sources to receivers. However, for reflection seismology, the reflective layers need to be accurately positioned in the subsurface to compute such raypath pairs. This induces possible imaging- and interpretation-based errors in the raypaths' calculation. For direct source-receiver acquisitions, such as cross hole, these error sources do not exist. Raypaths are calculated directly using the velocity field, which we assume is correct. Therefore, we elect to illustrate the method using a cross-hole example.

Recorded data were calculated using a full viscoelastic time-domain spectral elements scheme, following the approach suggested by Fan et al. (2016). Despite using the most recent modeling techniques, it is important to remember that accurate anelastic modeling, especially for low Q values, is still a subject of ongoing research. As previously stated, recorded data must be muted around the first arrivals. Several characteristic shot records, before (Figure 5a) and after (Figure 5b) such muting, are shown in Figure 5. The complex velocity model induces nonhyperbolic first-arrival traveltimes. Intrinsic attenuation affects wavelet smearing, and we can see extrinsic attenuation due to model complexity as random-like distortions in recorded wavefields.

We use muted shot records as input for two different inversions. The first is based on the reconstructed source consistency, whereas the second uses a conventional centroid frequency-shift objective function. In both cases, the optimization procedure was ACO with the same tuning parameters and run time, and the correct velocity model was used. The only difference was thus the used objective function. For the centroid frequency-shift case, we follow Quan and Harris (1997) and compute the objective function using the frequency center of mass value. It is calculated using a weighted frequency average with spectral amplitude as weights and yields a single parameter. The reconstructed source consistency objective function, on the contrary, is calculated using the entire frequency spectrum. In addition, the frequency-shift objective function operates on differences between the original (source) and recorded centroid frequency, whereas reconstructed source consistency is applied to back-propagated traces and does not require the source function.

Because the source spectrum is required when using the frequency-shift approach, we use the correct one. The Q model, used for forward modeling and inversion, is a complex structure, consisting of 11 different blocks. There is no initial model because each ant randomizes its own starting model and the only constraint is the Q range for each block, taken to be 5–70. After 500 iterations (colonies), each containing 20 ants, both solutions converged. In terms of run time, this is equivalent to a few hours on a single CPU. In Figure 6, we summarize the Q-inversion results. Using the source-
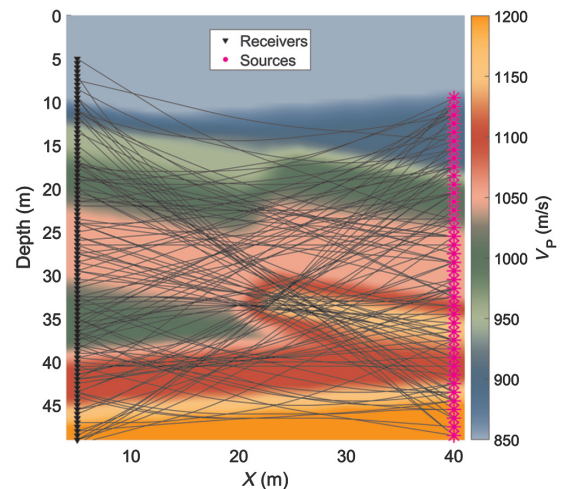

Figure 4. Synthetic cross-hole test. Sources are denoted by purple stars and receivers by black triangles. The underlying complex velocity model causes complex trajectories of source-receiver paths, some of which are displayed as black lines.
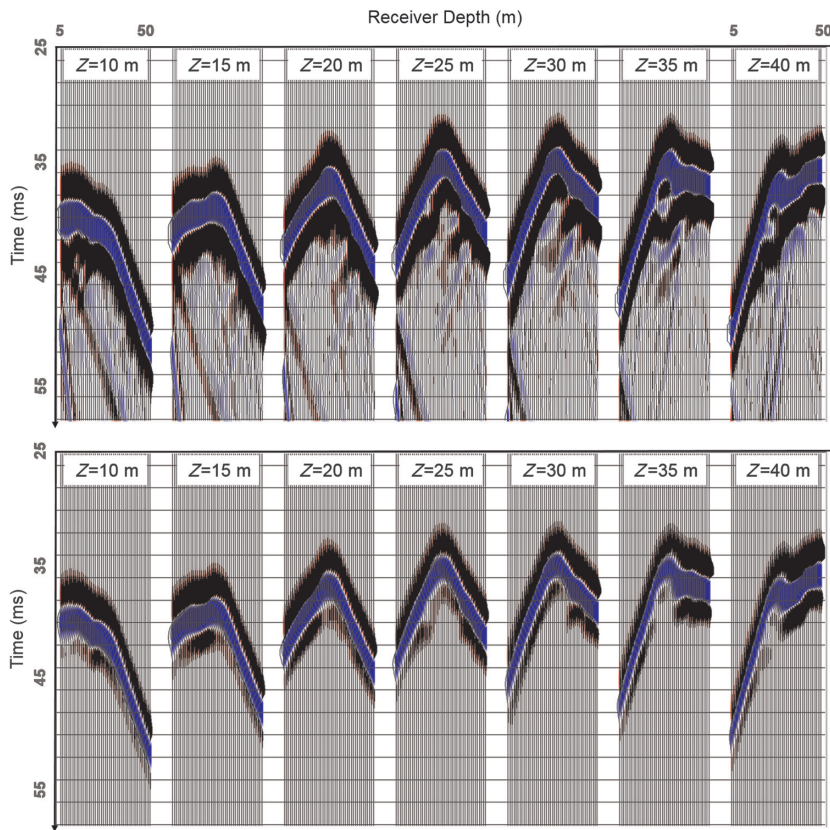
Figure 5. Modeled recorded data for representative shot records at different depths, (a) before and (b) after muting around first arrivals. Receiver depth ranges from 5 to 50 m. Due to the complex velocity structure, first arrivals are nonhyperbolic. Effects of intrinsic attenuation can be seen on the wavelet shape. Extrinsic attenuation, induced by structural inhomogeneity, is visible as random-like wavelet distortions, clearest after the first-arrival positive (blue) phase. Whereas muting eliminates later events, intrinsic attenuation clearly affects inversion input data.

consistency objective function, the inverted model is very close to the true one. However, when the conventional centroid frequency-shift measure is used, the inverted model is clearly erroneous. Because the only difference between the two inversions is the objective function, we conclude that the reconstructed source consistency objective function is clearly superior. The parametric reduction of the frequency-shift approach is insufficiently sensitive for high-resolution Q-model inversion. In addition, the source-consistency objective function does not require source knowledge information. For this comparison, it was known and correctly used as input for the frequency-shift approach. However, this is an unrealistic assumption in real-world applications, and it might thus induce further errors in the inversion procedure.

A comparison between the recorded and reconstructed source spectrum, using the Q model obtained with the reconstructed source consistency objective function, is shown in Figure 7. Recorded data have, as expected, a very inconsistent spectral shape. However, after their reconstruction at their original location using the inverted Q-model, they display a much more coherent behavior along receivers.

Nonetheless, inverted spectra are not perfectly coherent. This issue has several possible causes. The first, obvious, one is that the inverted model is not exactly equivalent to the true model. However, their difference is not substantial. A second, more prominent, cause is the well-known modeling inaccuracy. It is especially acute around regions of strong Q contrast, which often appear in
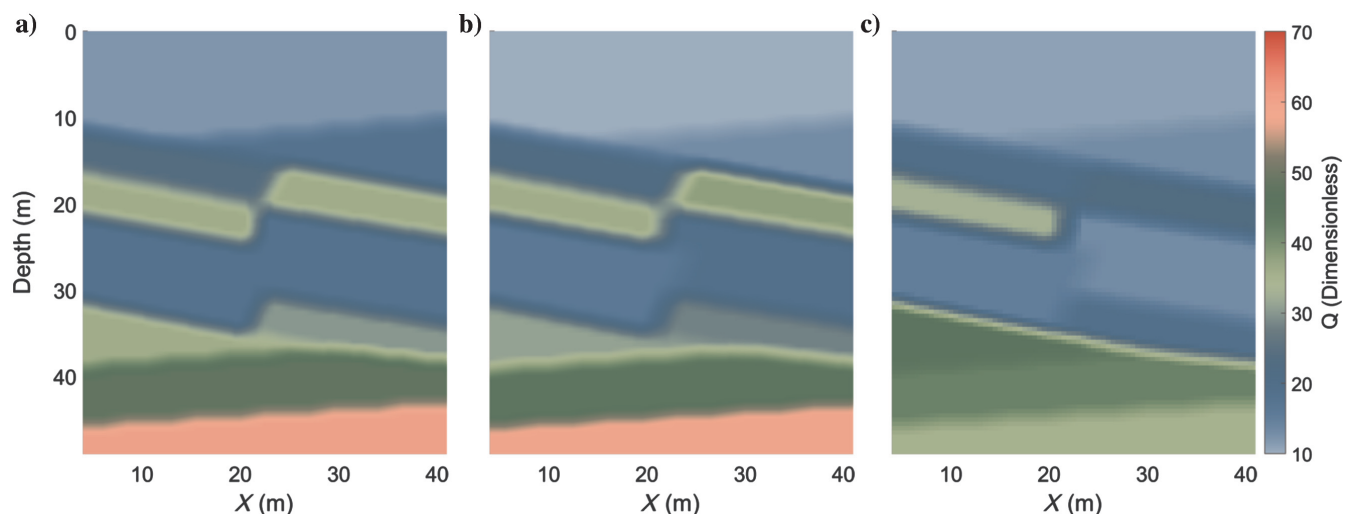

Figure 6. The Q-inversion results. The true model, used for creating the data shown in Figure 5, is shown in (a). It is complex and with sharp Q contrast. (b) The inverted model obtained using reconstructed source consistency is very close to the true model. (c) Using the frequency-shift objective function, on the contrary, yields a clearly erroneous model despite correct source spectrum information. Because, setting aside the objective function, all inversion parameters were equal, we conclude the superiority of the reconstructed source-consistency method.

our blocked model. Third, forward modeling is performed using an anelastic wave-equation formulation, whereas inversion is based on a tomographic ray-approximation approach. More specifically, extrinsic attenuation rising due to structural complexity cannot be computed by ray approximation. Therefore, the inversion formulation does not account for it, and it may thus compensate for its effect by wrongly altering the intrinsic attenuation field.

We suggest another approach to evaluating inversion results. Following FWI principles, we compare recorded and modeled data, computed with the Q model inverted for using the reconstructed source consistency objective function. It is important to note that because this example is synthetic, the recorded and modeled data are computed using the same wave-equation forward operator. For reference, we also compute modeled data for a background, constant $-Q$ model. We want to emphasize that although data-misfit minimization is a viable objective function, it was not used in our inversion scheme. In Figure 8, we summarize the comparison. We first show recorded data for a single shot at a depth of 20 m (Figure 8a). In Figure 8b, we show modeled data computed using the inverted Q model. Data are very similar to the recorded ones in terms of amplitude distribution and arrival traveltimes. In Figure 8c, we show data modeled with a constant $Q = 40$ model. Here, amplitudes are significantly different, and the entire wavefront is delayed by approximately 1 ms. This is indicative of a wrong Q model, influencing dissipation and dispersion. In Figure 8b2 and 8c2, we show the differences between modeled and recorded data. Using a constant Q model, the misfit is almost an order of magnitude more than when the inverted Q model is used. From this example, we deduce that our suggested inversion scheme is reliable, because it is verified and proved successful by an independent method.
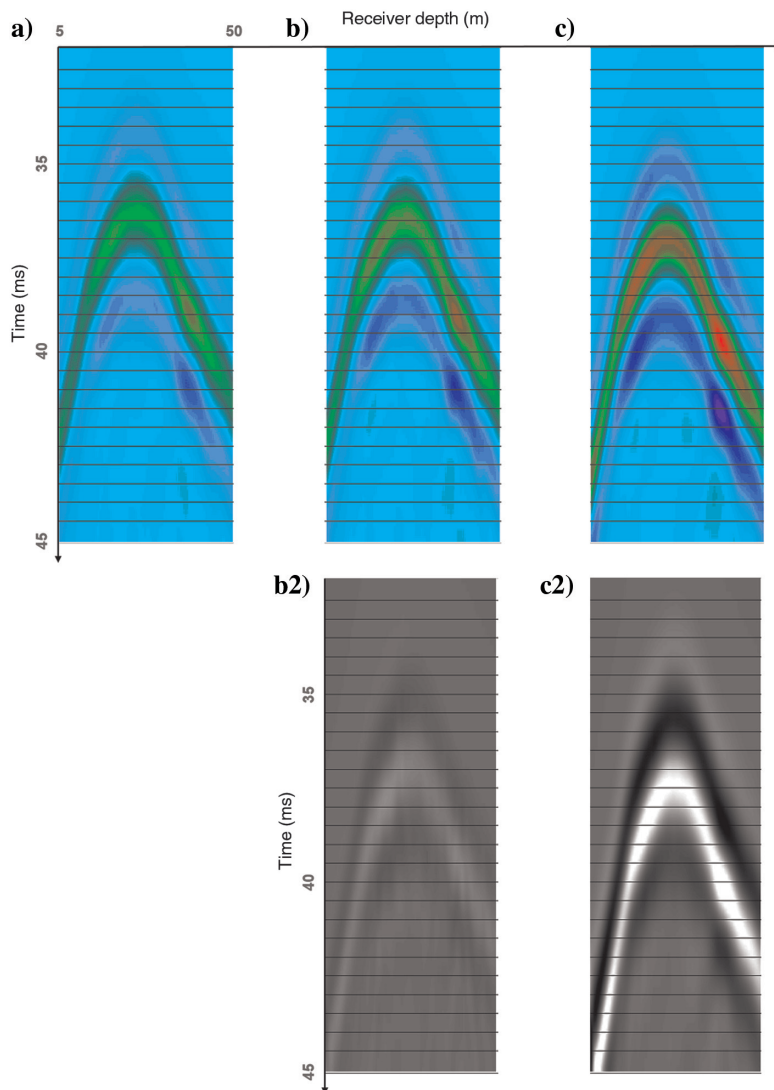

Figure 8. Comparison of recorded and modeled data, for a shot at 20 m depth. We show recorded data in (a). In (b), we display modeled data, obtained with the inverted Q model (Figure 6b). Modeled data with a constant $Q = 40$ model is in (c). Subplots (a-c) are normalized to the same scale. (b2 and c2) The differences between (b and a) and (c and a) are shown, accordingly. Again, (b2 and c2) are normalized to the same scale. Although waveform similarity was not the objective function, we can see an excellent match when the inverted model is used for modeling. The amplitudes and arrival traveltimes are similar. When a background model is used instead, the amplitude distribution is significantly different and the wavefront is delayed by approximately 1 ms.
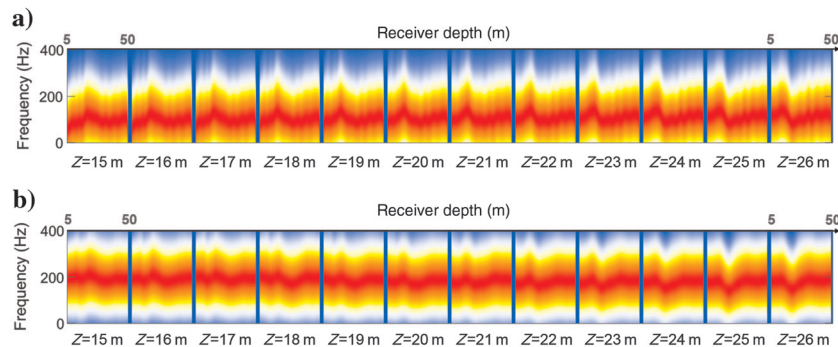

Figure 7. Recorded and reconstructed spectrums. (a) The originally recorded spectrum depicts representative consecutive shot records, laid one next to the other. The same shots' spectrum, after reconstruction at their location using the estimated Q model (see Figure 6b), is shown in (b). In the original spectrum, each shot is very inconsistent in its spectral shape (among different receivers). After reconstruction with the inverted Q model, discrepancy is minimized and the spectra are more consistent.

INVERSION STABILITY

Due to the random nature of global optimization, inversion results need to be checked for stability. This is especially important due to the complexity of the objective function, which contains many local minima. In addition, it is possible that different models might have a practically equivalent objective function value. Therefore, we perform 40 independent ACO runs and analyze inverted models as well as convergence curves. The same analysis is conducted for the reconstructed source consistency and frequency-shift objective functions. All runs were conducted with the same velocity model and ACO parameters (see Appendix A). Figure 9 summarizes these results. In Figure 9a, we show the stability of the inverted models using the reconstructed source consistency objective function. We take the pixel-by-pixel standard deviation of the inverted Q models (across 40 different ACO runs) and divide it by the mean estimated model. The resulting image is a good measure, in percentage, of the inverted models' stability. Setting aside the poorly covered top layer, the standard deviation is less than 10% for all blocks and approximately 5% average over the entire model. This indicates a stable inversion

procedure, despite the many difficulties previously discussed. Average convergence using reconstructed source consistency behaves (Figure 9b) as expected, with a fast initial improvement, curbing with time, and eventual convergence to a stable solution. However, by looking at its standard deviation, we can see that the large number of iterations is required to assure that all 40 ACO instances have indeed finished converging. When the frequency-shift objective function is used instead, stability issues arise. Inverted models (Figure 9c) may suffer from up to 30% standard deviation in certain areas, and inversion does not converge (Figure 9d). Despite an initial improvement, the objective function does not reach a stable solution. This is consistent with the high variation of the inverted models. Overall, we conclude the superiority of the reconstructed source consistency in terms of inverted models and their stability.

FIELD-DATA EXAMPLE

We tested the application of the method on a dense cross-hole survey acquired in the shallow subsurface section. The wells were interchangeable, each acting as source and receiver boreholes. We illustrate the
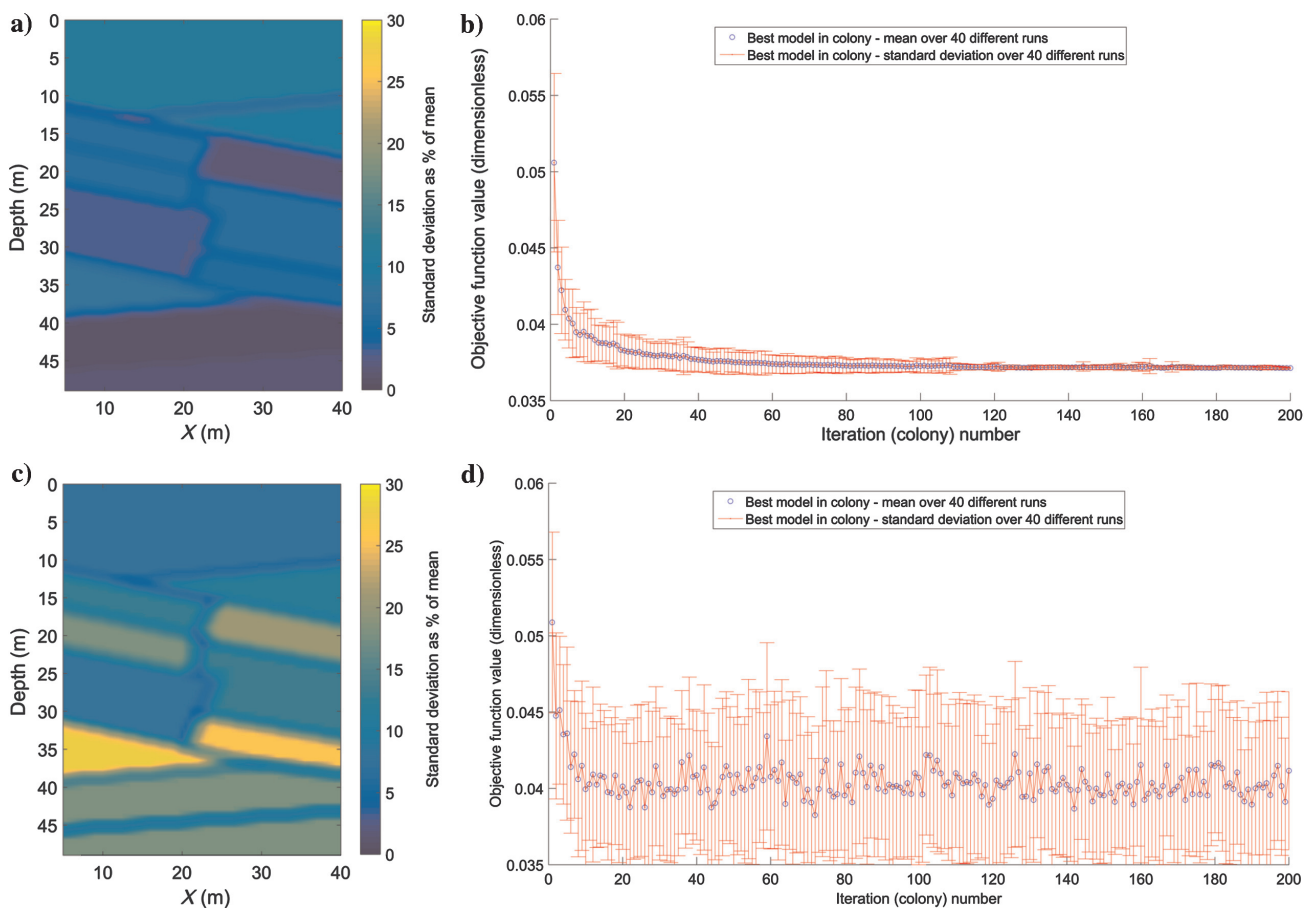

Figure 9. Stability and convergence analysis of the ACO method using different objective functions — reconstructed source consistency and frequency shift. For both cases, 40 different ACO runs were conducted, and their results and convergence curves analyzed. In (a), using reconstructed source consistency, we show the standard pixel-wise deviation, across different ACO runs, of inverted Q models, normalized by the mean estimated Q value model. Except the upper layer, which is poorly covered, the standard deviation is less than 10% in all areas, and its average is approximately 5%. In (b), we show the mean convergence graph of the reconstructed source-consistency inversion, with error bars indicating the standard deviation. The fastest increase is during the first 50 iterations (colonies), and the subsequent convergence is very slow. However, the standard deviation decreases, indicating that more and more different ACO instances are converging to a stable solution. In (c and d), we repeat the procedure with the conventional frequency-shift objective function. In this case, model standard deviation may reach almost 30% in certain areas and the objective function does not seem to converge, despite improving from the initial values. This indicates an unstable objective function, explanatory of high variance of inverted models.

survey's layout in Figure 10, along with the underlying velocity field estimated using conventional traveltime tomography. Because there were technical problems with some of the shots due to coupling/trigger issues, only acceptable source-receiver pairs are shown. In Figure 11, we show several characteristic shot records after a very coarse muting around the first arrivals. Since used downhole geophones have a uniaxial direction (*z*) of measurement, polarity reversal occurs. However, as the suggested approach operates solely in the frequency domain, it does not have any effect on the results. In the time domain, on the contrary, it could influence inversion methods based on time-domain amplitudes, such as rise time or amplitude decay (Tonn, 1991).

In Figure 12, we show inversion results using this data set. Although the data are noisier and limited to fewer than 200 traces, inversion does converge to a stable solution (Figure 12a). The overall trend is of *Q* strongly increasing with depth, which is consistent with the compaction model of loose sands present in the area. There are some mild lateral heterogeneities, as may be expected in the shallow subsurface section. We compare inversion results to a 1D *Q* model extracted at the left borehole using conventional check-shot frequency shift. For such an analysis, the method is very stable and reliable. Inversion is unreliable near the borehole due to coverage issues. Therefore, we compare the 2D result at a distance of approximately 5 m from the well. Taking into account the overall slope of the inverted model, the two results are close. By observing the recorded and reconstructed spectrum (Figure 13), we may evaluate the quality of the estimated model in a different way. First, the reconstructed spectrum has, as expected, a much higher frequency content. For most shots, the reconstructed spectral shape is rather consistent along different receivers. When it is not the case, it seems that discrepancies arise due to specific traces, which have an outlying spectral behavior before inversion. Therefore, we are confident that the estimated *Q* model, given the data quality and coverage, is reliable.

DISCUSSION

In this study, we suggest using the reconstructed source frequency consistency as an objective function for an inverse problem formulation of *Q*-factor estimation. It uses the entire spectrum rather than its parametric reduction, does not require the source function, and is based on simple data preprocessing. The used objective function's originality is that it avoids the conventional inversion approach of minimizing the discrepancy between recorded and modeled data, or some of their characteristics. Instead, it only incorporates self-consistency of back-propagated data, following the time-reversal principle. Finding its minimal value is formulated as a global optimization problem, solved using the ACO approach. It is also worth noting that a local optimization solution to the inversion problem can be formulated using a similar objective function, but it is prone to local minima convergence and dependency on the often poor initial *Q* model. This approach is currently under research and shows promising results.

A main assumption made using the suggested method is the correct velocity model, which is used for raypath calculation. As we show, *Q* estimation might suffer greatly if an incorrect velocity model is used. However, the correct

velocity assumption is commonly made. The reason is that a joint estimation of the two fields is practically difficult due to their inherent coupling. Therefore, we opt for an iterative, step-by-step approach, separating velocity from attenuation estimation.

The suggested approach is based on a ray-approximation tomographic equation. Although it has many practical benefits, it induces certain limitations that are important to recognize. These shortcomings are shared by all *Q*-tomography methods. First, such
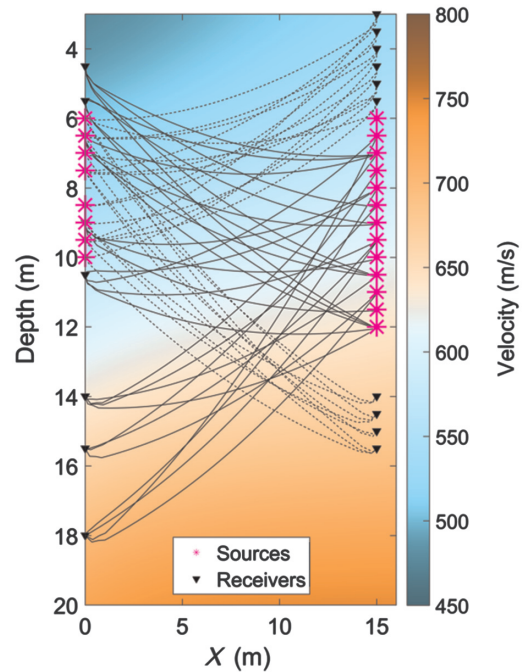

Figure 10. Field-data acquisition. Sources are denoted by purple stars and receivers by black triangles. The source and receiver boreholes have been inverted during acquisition to increase coverage. The P-wave velocity model displayed in the background was estimated using conventional traveltime tomography and was subsequently used for source-receiver path calculation (full/dashed black lines, according to the well of origin).
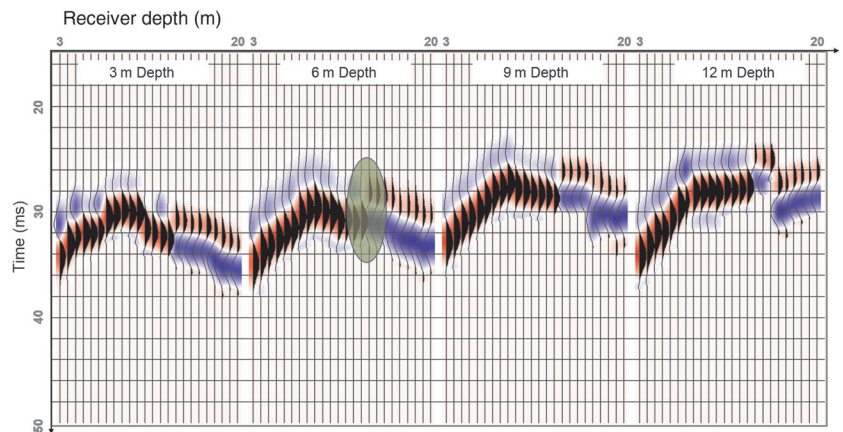

Figure 11. Shot records excited at different depths in right borehole (see Figure 10), coarsely muted around the first arrivals (P-waves). The moveout of the first arrivals is very complex due to the underlying velocity field. Due to the uniaxial (*z*-direction) recording of the downhole geophones, polarity reversal (marked, for exemplification, by a green ellipse) occurs in all records.

a formulation cannot account for extrinsic frequency-dependent attenuation caused by elastic propagation in a heterogeneous subsurface. In the presence of layers or scatterers, different wavelengths might behave dissimilarly, thus inducing extrinsic attenuation. The ray approximation is incapable of accounting for these effects. Therefore, an inversion scheme based upon it will wrongly alter the anelastic attenuation model Q in compensation. Second, as the ray approximation is also acoustic, solely single-mode seismic waves may be used. In this study, we limited ourselves to the first arrivals (P-waves). Set aside the information loss, it also requires muting the data around the first arrivals. Third, it commands application on smooth velocity models only, because ray tracing induces errors or, worse, does not reach its targets under the presence of complex

structures and sharp contrasts. We reiterate that these limitations are shared by most, if not all, conventional Q-tomography methods.

Nonetheless, using a wave-equation approach is practically difficult. Precisely incorporating anelastic effects into the modeling scheme, being forward or backward, is still a subject of ongoing research because it suffers from instability (Yang et al., 2016). Conventional methods induce at least several percent errors (Fan et al., 2016) and further deteriorate for low Q values, such as the ones handled in this study. The error is not necessarily symmetric for the forward and back propagation. In addition, computation times are significantly increased, especially when relatively high precision is required. Nonetheless, time-harmonic methods (Operto et al., 2007) may be used to accurately and efficiently perform the calculations, but they require extensive memory. On the contrary, using a ray-approximation approach, paths need to be calculated only once using the velocity model. Subsequently applying different Q models is extremely fast because it amounts to matrix (raypaths) by vector (Q^{-1} model) multiplication. For wave-equation methods, the full propagation has to be conducted for every different Q model. Because global optimization requires numerous objective function estimations, a wave-equation approach would be impractical given our computational means. Finally, the fact that wave equation propagation can handle structure-induced extrinsic attenuation may be a practical difficulty. Whereas ray tracing requires an acceptable smooth velocity model, the wave equation requires an accurate description of the subsurface in terms of density and elastic parameters, a much more difficult task. Moreover, such a description has to accurately represent contrast to correctly predict amplitudes and their frequency dependence, and coupling problems will arise if such a representation is incorrect.
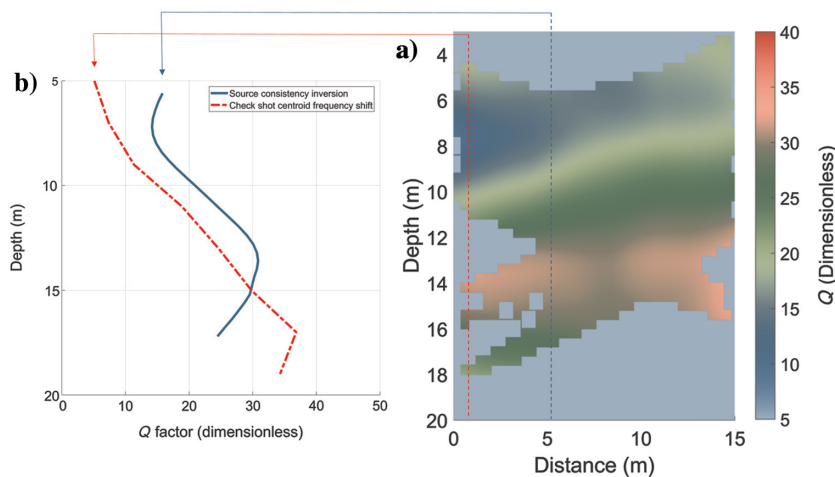
Global optimization has it downsides, and the used algorithm is no different. It is more computationally demanding and harder to reproduce because it involves random processes. Due to high computational requirements, it is effectively limited by the complexity of the models it can represent. This restriction is especially noticeable in cases of laterally varying 3D models. By increasing computational resources, more detailed models can be inverted for. Notwithstanding, in our suggested approach, Q is estimated only after a velocity model, and possibly structural image, has been constructed. Using an interpretation-based process, it is possible to represent the Q field with a relatively small amount of regions, which can be then inverted for using global optimization. Of course, stability and convergence remain a problem-dependent issue, but we have shown positive signs of a stable inversion.

Therefore, we suggest using this method as another step in an iterative process aiming for a correct anelastic representation of the subsurface. The first stage would be conventional velocity analysis, followed by an interpretation-driven

Figure 12. (a) Inverted Q model using field data. Coverage issues are clearly present, and not all the area between the boreholes is resolved. However, a strongly increasing with depth Q is visible. Lateral heterogeneity is not negligible, but it is much less prominent than the depth variation. The model estimated at the dotted blue line location is compared with a conventional checkshot (1D) frequency-shift analysis (b). Taking into account the apparent slope of the model, the difference between the well log and the sliced inversion result, located at 5 m distance, is reasonable.
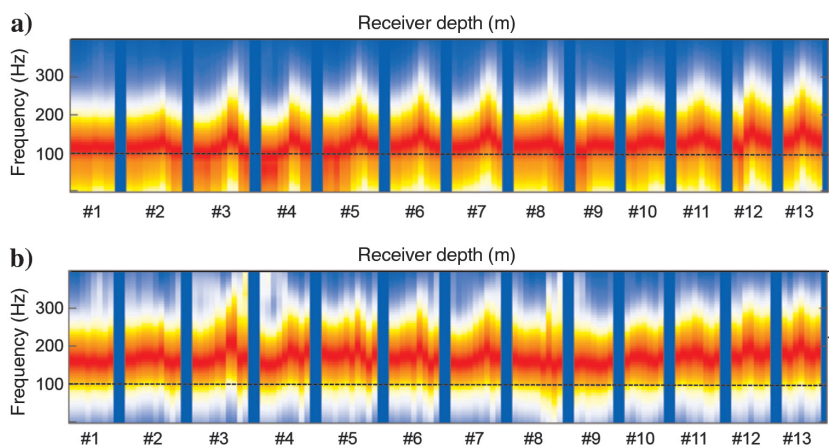

Figure 13. Recorded and reconstructed spectrums. The 100 Hz line is marked in both using a dashed line. (a) The recorded spectrum contains significant low-frequency (<100 Hz) energy, and there is a large inconsistency between spectral shapes among different receiver traces of each shot. After source reconstruction using the inverted Q model (Figure 12), (b) the spectral shapes have a higher frequency content and are more consistent. However, some local discrepancies, visible in the original recorded spectrum, are not resolved by the inversion.

Q skeleton model construction. Then, our suggested method would be applied. At this point, reasonable velocity and *Q* models would be available. They may be used as a basis for viscoelastic FWI, jointly with a density model if present. Alternatively, it would be possible to first improve velocity model precision by incorporating second-order corrections due to anelastic dispersion. Subsequently, a refined *Q* model will be estimated on the basis of new raypaths calculated from the updated velocity model, and so forth.

In this study, we aim at illustrating the advantages of reconstructed source consistency objective function, and therefore we chose direct source-receiver paths examples. However, its extension to surface data and reflection events should be the focus of future research. As inversion is formulated on the basis of raypaths, the only difference in its application would be constructing source-receiver paths as a combination of two rays — source to reflection point and reflection point to receiver. This requires a correct estimation of reflection horizons. Naturally, interpretation errors are possible, and velocity errors would see their impact enhanced. An additional limitation of using the method with conventional reflection data is the underlying *Q* model complexity, which is difficult to represent using a relatively small number of parameters. However, as the method would be applied after initial structural imaging, an interpretation-based *Q* model parameterization could again prove useful. For most cases, tens to several hundreds of regions, each with its own *Q* value, could probably be reliably inverted. At this point, resulting models could be a basis for anelastic FWI, or first iteratively recomputed with anelastic corrections to the velocity and raypath estimation, followed by a new *Q* model inversion.

CONCLUSION

In this study, we suggest using the reconstructed source-frequency consistency as a novel objective function for an inverse problem formulation of *Q*-factor estimation. It uses the entire spectrum rather than its parametric reduction, does not require prior knowledge of the source function nor its inversion, and is fully automatic once basic preprocessing has been applied. It is formulated as a global optimization problem, solved using the ACO approach. The source function, useful for other procedures, can be reliably obtained as a byproduct of the method.

Using a complex synthetic cross-hole example, we show the accuracy, stability, and convergence of our suggested approach in recovering a strongly varying *Q*-model. The same inversion scheme fails when a conventional centroid frequency shift objective function is used, despite using the correct additional information of source spectrum. We thus conclude the superiority of the reconstructed source-frequency consistency objective function. When applied to a challenging field cross-hole example, it performs well even under the limitations of scarce data and mediocre coverage. Inversion results are compared with a conventional, reliable check-shot 1D model, and are highly compatible. In both examples, the reconstructed spectra consistency is indicative of estimated model quality.

The suggested method makes several assumptions. First, it assumes a known and correct underlying velocity model. Second, it uses a ray approximation to the wave equation. This limits its ability to compute raypaths in complex models, and it cannot correctly take into account extrinsic attenuation. Finally, due to the global optimization parameterization, it is limited in the detail of models it can invert for. On the other hand, it successfully converges despite a complex, multimodal, and velocity-coupled objective function.

Although both illustrative examples are of cross-hole acquisition, the method may be applied to any acquisition geometry in which source-receiver paths are known, e.g., reflection seismology. Naturally, complexity would be increased and interpretation-based procedures would have to be used to build reasonable *Q* skeleton models. Nonetheless, we believe that the suggested approach should be used as part of an iterative process, either for cross hole or surface acquisition, whose results may be an initial model for anelastic FWI.

DATA AND MATERIALS AVAILABILITY

Data associated with this research are available and can be obtained by contacting the corresponding author.

APPENDIX A

ANT-COLONY OPTIMIZATION

The ant-colony system optimization was first introduced by Dorigo (1992) and Dorigo and Di Caro (1999) as a method for solving complicated combinatorial optimization problems, and it was later extended to continuous domains (Socha and Dorigo, 2008). It is a probability-driven method that was inspired by observing ant foraging behavior. There are many variations of this method (Dorigo and Gambardella, 1997; Stützle and Hoos, 2000), all based on the same principle. It incorporates two basic steps that are been iteratively applied until convergence:

1) generating a set of solutions
2) pheromone update.

The first step consists of generating a set of *C* solutions (*C* is the number of ants) S_c, drawn from the full search space S_P. The solution is generated following the probability density function (PDF) $P(S_P)$. In the first iteration, $P(S_P)$ is set to be uniform; hence, the search is random. After the first set of solutions is generated, pheromones, and accordingly $P(S_P)$, are updated. This step's goal is to increase the pheromone density around promising solutions and decrease their level around poor solutions. Thus, the probability to search around the true solution will increase in subsequently generated models. Such a goal is obtained by introducing pheromones τ_{ij}, which influence $P(S_P)$. They are updated for each iteration (known as a colony), according to the following rule:

$$\tau_{ij} = \begin{cases} (1-\rho)\tau_{ij} + \rho\Delta t & \text{if } \tau_{ij} \in s_{B,} \\ (1-\rho)\tau_{ij} & \text{otherwise.} \end{cases} \quad \text{(A-1)}$$

Updates depend on Δt, which is an objective function measure, and an evaporation preset parameter $\rho(0 \leq \rho \leq 1)$. The objective function used in this study was $1 - E(f)^{1/4}$, introduced in equation 6. It is important to note that Δt influences the pheromone τ_{ij} is the condition $\tau_{ij} \in s_B$ is fulfilled, meaning that the pheromone is associated with the best model S_B. There are two common approaches in choosing S_B. The first is the "best-so-far approach," which sets S_B as the

best overall solution, in terms of objective function, found since the beginning of the run. The second approach is the "iteration-best approach," which sets S_B as the best solution obtained from the current colony (iteration). The evaporation parameter ρ controls the trade-off between keeping the best model only, for a single next colony ($\rho = 1$), and completely disregarding the objective function and applying random search ($\rho = 0$). In this study, we chose a relatively high value of $\rho = 0.3$ to quickly extinguish poor solutions.

The PDF of drawing a model C_{ij}, after the pheromone update stage, is given by

$$P(C_{ij}) = \frac{[\tau_{ij}]^\alpha [\eta(C_{ij})]^\beta}{\sum_{C_{ij}} [\tau_{ij}]^\alpha [\eta(C_{ij})]^\beta}, \quad \forall\, C_{ij} \in S_P, \qquad \text{(A-2)}$$

where η represents a priori information about the search space. Parameters α and β are positive factors used for trade-off between a priori knowledge and pheromone, or objective function-based, information. As in many heuristic optimization methods, and in particular in probabilistic global optimization ones, parameter choice is crucial and is a problem-dependent issue. In this case, we had neither a priori information about the solution (expect lower and upper bounds) not any heuristic preference, and thus set η, α, β as one.

Finally, we incorporate a random, pheromone-independent model generation option. In this study, 10% of model generations are drawn randomly from a uniform distribution. The goal of this modification is to allow for uncharted, remote areas of the objective function to be explored.

REFERENCES

Aki, K., and P. G. Richards, 2002, Quantitative seismology: University Science Books.

Blias, E., 2012, Accurate interval Q-factor estimation from VSP data: Geophysics, **77**, no. 3, WA149–WA156, doi: 10.1190/geo2011-0270.1.

Brzostowski, M. A., and G. A. Mcmechan, 1992, 3-D tomographic imaging of near-surface seismic velocity and attenuation: Geophysics, **57**, 396–403, doi: 10.1190/1.1443254.

Carcione, J. M., F. Cavallini, F. Mainardi, and A. Hanyga, 2002, Time-domain modeling of constant-Q seismic waves using fractional derivatives: Pure and Applied Geophysics, **159**, 1719–1736, doi: 10.1007/s00024-002-8705-z.

Cavalca, M., I. Moore, L. Zhang, S. L. Ng, R. Fletcher, and M. Bayly, 2011, Ray-based tomography for Q estimation and Q compensation in complex media: 81st Annual International Meeting, SEG, Expanded Abstracts, 3989–3993, doi: 10.1190/1.3628039.

da Silva, N. V., G. Yao, M. Warner, A. Umpleby, and H. Debens, 2017, Global visco-acoustic full waveform inversion: 79th Annual International Conference and Exhibition, EAGE, Extended Abstracts, doi: 10.3997/2214-4609.201700504.

Dorigo, M., 1992, Optimization, learning and natural algorithms: Ph.D. thesis, Politecnico di Milano.

Dorigo, M., and G. Di Caro, 1999, Ant colony optimization: A new meta-heuristic: Proceedings of the Congress on Evolutionary Computation, 1470–1477, doi: 10.1109/CEC.1999.782657.

Dorigo, M., and L. M. Gambardella, 1997, Ant colony system: A cooperative learning approach to the traveling salesman problem: IEEE Transactions on Evolutionary Computations, **1**, 53–66, doi: 10.1109/4235.585892.

Dutta, G., and G. T. Schuster, 2016, Wave-equation Q tomography: Geophysics, **81**, no. 6, R471–R484, doi: 10.1190/geo2016-0081.1.

Fan, N., L. F. Zhao, X. B. Xie, Z. Ge, and Z. X. Yao, 2016, Two-dimensional time-domain finite-difference modeling for viscoelastic seismic wave propagation: Geophysical Journal International, **206**, 1539–1551, doi: 10.1093/gji/ggw228.

Hak, B., and W. A. Mulder, 2011, Seismic attenuation imaging with causality: Geophysical Journal International, **184**, 439–451, doi: 10.1111/j.1365-246X.2010.04848.x.

Harris, P. E., C. Kerner, and R. E. White, 1997, Multichannel estimation of frequency-dependent Q from VSP data: Geophysical Prospecting, **45**, 87–109, doi: 10.1111/j.1365-2478.1997.tb02272.x.

Hu, W., J. Liu, L. Bear, and C. Marcinkovich, 2011, A robust and accurate seismic attenuation tomography algorithm: 81st Annual International Meeting, SEG, Expanded Abstracts, 2727–2731, doi: 10.1190/1.3627760.

Kjartansson, E., 1979, Constant Q-wave propagation and attenuation: Journal of Geophysical Research, **84**, 4137–4748, doi: 10.1029/JB084iB09p04737.

Kurzmann, A., A. Przebindowska, D. Köhn, and T. Bohlen, 2013, Acoustic full waveform tomography in the presence of attenuation: A sensitivity analysis: Geophysical Journal International, **195**, 985–1000, doi: 10.1093/gji/ggt305.

Landa, E., W. Beydoun, and A. Tarantola, 1989, Reference velocity model estimation from prestacked waveforms: Coherency optimization by simulated annealing: Geophysics, **54**, 984–990, doi: 10.1190/1.1442741.

Lellouch, A., and E. Landa, 2017, Time reversal focusing for velocity estimation: Cross-well acquisition: 87th Annual International Meeting, SEG, Expanded Abstracts, 5620–5624, doi: 10.1190/segam2017-17632416.1.

Lellouch, A., and E. Landa, 2018, Seismic velocity estimation using time-reversal focusing: Geophysics, **83**, no. 4, U43–U50, doi: 10.1190/GEO2017-0569.1.

Liner, C. L., 2012, Elements of seismic dispersion: A somewhat practical guide to frequency-dependent phenomena: SEG.

Liu, H., D. L. Anderson, and H. Kanamori, 1976, Velocity dispersion due to anelasticity: Implications for seismology and mantle composition: Geophysical Journal of the Royal Astronomical Society, **47**, 41–58, doi: 10.1111/j.1365-246X.1976.tb01261.x.

Malinowski, M., S. Operto, and A. Ribodetti, 2011, High-resolution seismic attenuation imaging from wide-aperture onshore data by visco-acoustic frequency-domain full-waveform inversion: Geophysical Journal International, **186**, 1179–1204, doi: 10.1111/j.1365-246X.2011.05098.x.

Mulder, W. A., and B. Hak, 2009, An ambiguity in attenuation scattering imaging: Geophysical Journal International, **178**, 1614–1624, doi: 10.1111/j.1365-246X.2009.04253.x.

Operto, S., J. Virieux, P. Amestoy, J.-Y. L'Excellent, L. Giraud, and H. B. H. Ali, 2007, 3D finite-difference frequency-domain modeling of visco-acoustic wave propagation using a massively parallel direct solver: A feasibility study: Geophysics, **72**, no. 5, SM195–SM211, doi: 10.1190/1.2759835.

Quan, Y., and J. M. Harris, 1997, Seismic attenuation tomography using the frequency shift method: Geophysics, **62**, 895–905, doi: 10.1190/1.1444197.

Ribodetti, A., S. Operto, J. Virieux, G. Lambaré, H. P. Valéro, and D. Gibert, 2000, Asymptotic viscoacoustic diffraction tomography of ultrasonic laboratory data: A tool for rock properties analysis: Geophysical Journal International, **140**, 324–340, doi: 10.1046/j.1365-246x.2000.00015.x.

Sen, M. K., and P. L. Stoffa, 2013, Global optimization methods in geophysical inversion: Cambridge University Press.

Shen, Y., B. Biondi, and R. Clapp, 2015, Wave-equation based Q tomography from angle-domain common image gathers: 85th Annual International Meeting, SEG, Expanded Abstracts, 4334–4338, doi: 10.1190/segam2015-5917329.1.

Shustak, M., and E. Landa, 2017, Time reversal diffractor detector: 87th Annual International Meeting, SEG, Expanded Abstracts, 969–973, doi: 10.1190/segam2017-17640587.1.

Shustak, M., A. Lellouch, E. Landa, and M. Reshef, 2017, Q-factor estimation using reconstructed source consistency inversion: 79th Annual International Conference and Exhibition, EAGE, Extended Abstracts, doi: 10.3997/2214-4609.201701155.

Socha, K., and M. Dorigo, 2008, Ant colony optimization for continuous domains: European Journal of Operational Research, **185**, 1155–1173, doi: 10.1016/j.ejor.2006.06.046.

Stützle, T., and H. H. Hoos, 2000, MAX-MIN ant system: Future Generation Computer Systems, **16**, 889–914, doi: 10.1016/S0167-739X(00)00043-1.

Tonn, R., 1991, The determination of the seismic quality factor Q from VSP data: A comparison of different computational methods: Geophysical Prospecting, **39**, 1–27, doi: 10.1111/j.1365-2478.1991.tb00298.x.

van der Baan, M., 2012, Bandwidth enhancement: Inverse Q filtering or time-varying Wiener deconvolution?: Geophysics, **77**, no. 4, V133–V142, doi: 10.1190/geo2011-0500.1.

Wang, M., G. Li, H. Zheng, and T. Zhai, 2016, Estimating near-surface Q value based on the centroid frequency shift and integral area of the logarithmic spectral: 86th Annual International Meeting, SEG, Expanded Abstracts, 2449–2453, doi: 10.1190/segam2016-13772888.1.

Wang, S., D. Yang, J. Li, and H. Song, 2015, Q factor estimation based on the method of logarithmic spectral area difference: Geophysics, **80**, no. 6, V157–V171, doi: 10.1190/geo2014-0257.1.

Wang, Y., 2006, Inverse Q-filter for seismic resolution enhancement: Geophysics, **71**, no. 3, V51–V60, doi: 10.1190/1.2192912.

Wang, Y., 2009, Seismic inverse Q filtering: Blackwell Publishing.

Yang, P., R. Brossier, L. Métivier, and J. Virieux, 2016, Wavefield reconstruction in attenuating media: A checkpointing-assisted reverse-forward simulation method: Geophysics, **81**, no. 6, R349–R362, doi: 10.1190/geo2016-0082.1.